

# Ultrawide-band silicon microring avalanche photodiode with linear photocurrent-wavelength response

YANG REN\* AND VIEN VAN

Department of Electrical and Computer Engineering, University of Alberta, Edmonton, Alberta T6G 2W3, Canada

\*Corresponding author: yr@ualberta.ca

Received 20 July 2021; revised 4 September 2021; accepted 6 September 2021; posted 9 September 2021 (Doc. ID 437576); published 28 October 2021

We report a CMOS-compatible silicon microring-enhanced avalanche photodiode based on linear defect-state absorption in a  $p^+pn^+$  junction, with high responsivities exceeding 1 A/W at telecommunication wavelengths. The large photogenerated currents give rise to giant thermo-optic nonlinearity in the microring resonator, resulting in a linear photocurrent-wavelength response spanning the full free spectral range of the microring. This unique photocurrent spectrum could enable novel applications in wavelength-resolved photodetection, such as compact on-chip spectrometers, linear chirp frequency laser source characterization, and low-cost refractometric sensors without requiring precise wavelength-tunable lasers. © 2021 Chinese Laser Press

<https://doi.org/10.1364/PRJ.437576>

## 1. INTRODUCTION

With the advent of silicon (Si) photonics technology, there has been an increasing need for all-Si photodiodes (PDs) at the telecommunication wavelengths that are fully CMOS-compatible and can be monolithically integrated with other Si photonic components. As the bandgap wavelength of Si is around 1.1  $\mu\text{m}$ , photodetection based on linear photon absorption in Si material at telecommunication wavelengths is very inefficient, thus necessitating the use of Ge-doped Si or Ge-on-Si PDs in most applications [1–3]. Si PDs based on two-photon absorption (TPA), on the other hand, do not require Ge, but these devices suffer from low responsivities and nonlinear current-optical power characteristics [4]. Photodetection in Si pin and pn junctions based on defect state absorption (DSA), where the defects are specially implanted [5–8] or comprise the same doping impurities (boron and phosphorus) available during the formation of diode junctions in the conventional CMOS process [9–12], can have good current-power linearity and high bandwidth operations similar to Ge–Si PDs. For example, Si pin diodes implanted with  $\text{Si}^+$  ions could achieve internal quantum efficiencies up to 10 A/W [7], and high-energy boron-implanted pin junctions operating in avalanche mode were shown to have a responsivity of 4.7 A/W [6]. However, these devices require special processing steps that may not be available in standard SOI fabrication foundries. Si PDs that rely on defects introduced in the same steps used to form the junctions are fully CMOS-compatible but tend to suffer from low responsivities in the range of mA/W [12,13].

One way to increase the responsivities of these PDs is to enhance the optical field using a cavity such as a microring resonator. All-Si microring PDs embedded with pn or pin junctions have been reported to achieve peak responsivities up to 180 mA/W [4]. However, the use of a high-Q resonator limits the bandwidths of these PDs to less than 1 nm [12]. In addition, the sharp resonance spectrum of the microring and bistability effects caused by thermo-optic nonlinearity can render the performance of these devices unstable and sensitive to the wavelength and power of the optical signal [4]. On the other hand, the nonlinear interaction between the photocurrent and the optical power in the resonator can give rise to novel spectral characteristics not achievable in conventional PDs.

In this paper, we report a Si microring-enhanced avalanche PD (MR APD) based on DSA with unique linear photocurrent-wavelength response spanning the full free spectral range (FSR) of the microring resonator. The device is based on a separate absorption and multiplication (SAM) APD  $p^+pn^+$  junction embedded in a microring resonator and is fully compatible with the standard CMOS process. The strong field enhancement in the microring resonator combined with the large DSA in the p-doped absorption region results in large photocurrents near the breakdown voltage, with peak responsivities exceeding 1.5 A/W, which to our knowledge is the highest reported to date for CMOS-compatible Si PDs operating at 1.55  $\mu\text{m}$  wavelength. The large photogenerated currents give rise to unprecedented giant thermo-optic nonlinearity in the microring resonator, resulting in a remarkably linear photocurrent spectrum far exceeding the linear resonance linewidth of

the resonator. This unique photocurrent-wavelength response of the MR APD could enable novel applications requiring wavelength-resolved photodetection, such as compact on-chip spectrometer for wavelength monitoring, characterization of frequency chirped laser sources, and refractometric sensors without requiring precise tunable laser sources.

## 2. DESIGN OF Si MR APD

The Si MR APD consists of a  $p^+pn^+$  junction embedded in a Si-on-insulator (SOI) rib waveguide, as shown in Fig. 1(a). The rib waveguide is designed for TE polarization operation, with a core width of 500 nm, rib height of 130 nm, and slab thickness of 90 nm, lying on a 2  $\mu\text{m}$ -thick  $\text{SiO}_2$  layer [Fig. 1(b)]. The middle absorption region of the PD is centered over the waveguide core, with a width of 1.8  $\mu\text{m}$  and p-type doping concentration of  $3 \times 10^{17} \text{ cm}^{-3}$ . The role of the p-type impurities is to help increase electron hole pair generation by DSA. The  $p^+$  and  $n^+$  regions on both sides are heavily doped with concentrations of  $2 \times 10^{20} \text{ cm}^{-3}$  and  $5 \times 10^{20} \text{ cm}^{-3}$ , respectively, with the metal contacts to the anode and cathode separated by 5  $\mu\text{m}$ . The  $pn^+$  junction, where impact ionization takes place, is located in the thin slab region of the rib waveguide 650 nm from the core. Even near breakdown voltage ( $\sim 15 \text{ V}$ ), the depletion width is estimated to be less than 300 nm, so that the impact ionization region remains in the thin slab and is separated from the waveguide core where most of the light absorption takes place. Our device thus has the structure of an SAM APD [14,15]. In an SAM PD, the photocurrent is primarily due to free electrons that diffuse from the p-doped absorption region to reach the depletion region, where they are accelerated by the high electric field to ionize more electrons.

The  $p^+pn^+$  junction with a total length  $L_{\text{PD}} = 91 \mu\text{m}$  is embedded in a microring resonator with a 20  $\mu\text{m}$  radius. The microring is coupled to a straight rib waveguide through a gap of 300 nm. The straight waveguide is extended to the edges of the chip, where it is tapered to a width of 200 nm for butt-coupling with lensed fibers. An image of the fabricated device is shown in Fig. 1(c). Figure 2(a) shows the measured TE transmission spectrum of the microring around 1522.2 nm resonance wavelength at 0 V bias and low input optical power ( $\sim 100 \mu\text{W}$ ). By performing curve fitting to the measured

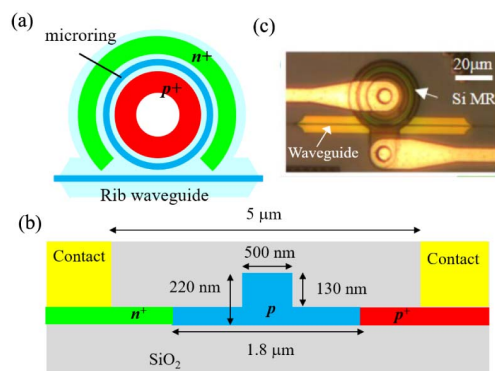


**Fig. 1.** (a) Design of the MR APD and (b) schematic of the Si rib waveguide embedded with a  $p^+pn^+$  junction; (c) optical microscope image of the MR APD.

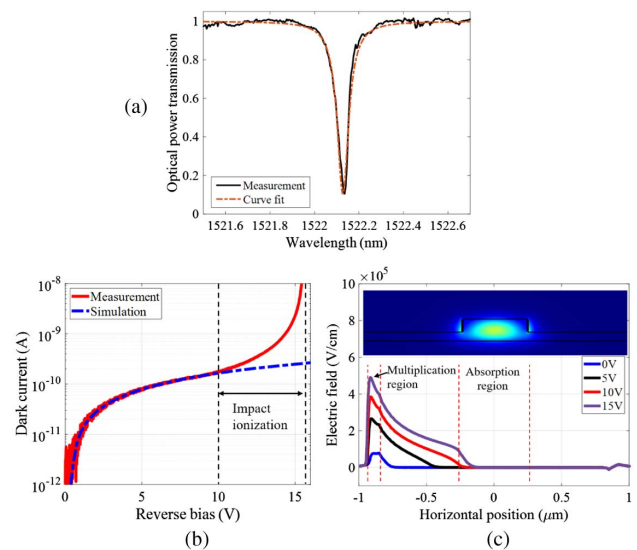


**Fig. 2.** (a) Linear resonance transmission spectrum of the microring at 0 V bias ( $\sim 100 \mu\text{W}$  input optical power); (b) measured and simulated dark current-voltage characteristics of the MR APD under reverse bias. The simulated current did not account for impact ionization. (c) Simulated electric field profiles across the  $p^+pn^+$  junction in the SOI waveguide. The upper panel shows the optical mode in the waveguide.

spectrum, we extracted the power coupling coefficient and propagation loss of the microring to be  $\kappa^2 = 2.74\%$  and  $\alpha = 1.6 \text{ dB/mm}$ , respectively. The high propagation loss can be attributed to the high impurity concentration in the p-type waveguide core. The microring has an FSR of 4.67 nm and a  $Q$  factor of 27,600, yielding an intensity enhancement of 20.7 times in the microring at resonance. Figure 2(b) shows the measured dark current versus the reverse bias voltage  $V_b$  of the MR APD. We observe that the dark current remains low ( $< 0.1 \text{ nA}$ ) until about 10 V, when it starts to increase significantly due to the onset of impact ionization. We also plot in Fig. 2(b) the simulated diode current of the  $p^+pn^+$  junction as a function of the reverse bias using the Lumerical software [16]. The measured and simulated curves are seen to have good agreement at low bias voltages up to about 10 V, when the measured current begins to rise significantly above the simulated current. As the simulation does not take into account impact ionization, the increase in the measured current can be attributed to gain due to impact ionization. Figure 2(c) depicts the simulated electric field profiles across the  $p^+pn^+$  junction, from which we observe that the electric field across the  $pn^+$  depletion region peaks at about  $4 \times 10^5 \text{ V/cm}$  at 10 V, when impact ionization starts to occur. This is also consistent with the ionization rate analysis reported in previous works [17,18].

As will be shown below, under illumination, the photocurrent of the MR APD depends on both the bias voltage and the optical power in the microring, so it is not straightforward to determine the multiplication factor of the MR APD due to impact ionization in the avalanche regime. We may, however, obtain an estimate of the multiplication factor from the dark

current curve in Fig. 2(b). Taking the unity gain bias voltage as 10 V where the current begins to increase due to impact ionization, we estimate the multiplication factor of the MR APD to be about 16 times at an operating bias voltage of 15 V.

### 3. PERFORMANCE CHARACTERISTICS OF THE MR APD

The photodetection performance of the MR APD depends strongly on the resonance spectrum of light inside the microring resonator. For the MR APD, the resonance spectrum is significantly modified from the linear resonance spectrum in Fig. 2(a) due to strong optical nonlinearity induced by free carrier (FC) dispersion and the thermo-optic effect in the Si waveguide. We first measured the optical transmission response of the MR APD by coupling TE-polarized light from a tunable laser to the input waveguide. Figures 3(a) and 3(b) show the transmitted optical spectra swept over the 1522.2 nm resonance for different input optical powers  $P_{in}$  in the input waveguide at reverse bias voltages of 0 V and 15 V, respectively. The corresponding photocurrent spectra are shown in Figs. 3(c) and 3(d). In both Figs. 3(a) and 3(b), we observe a redshift in the resonance dip and significant skewing of the resonance spectrum as the optical power is increased. This is caused by a nonlinear refractive index change in the microring due to the thermo-optic effect, which arises from ohmic heating of the Si waveguide by the generated photocurrent. We model the nonlinear effects in the microring by assuming that the round-trip phase  $\phi_{rt}$  and attenuation  $a_{rt}$  of the field in the microring depend on the generated photocurrent  $I_{ph}$ , which in turn depends on the optical power  $P_r$  inside the microring. Specifically, we express the round-trip phase as  $\phi_{rt} = \phi_L + \phi_{NL}$ , where  $\phi_L = -2\pi\Delta\lambda/\text{FSR}$  is the phase detuning from the linear resonance, and  $\phi_{NL}$  is the nonlinear phase shift, which is assumed to have a power dependence on the photocurrent as  $\phi_{NL} = \gamma I_{ph}^n$ . The photocurrent in general consists of two components: one due to TPA, which varies quadratically with  $P_r$ , and one due to DSA, which varies linearly with  $P_r$  [12,13].

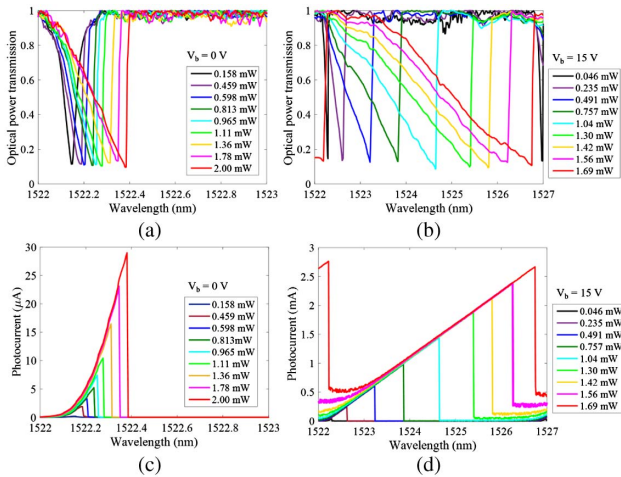


**Fig. 3.** Optical transmission spectra of the MR APD near the 1522.2 nm resonance for increasing input optical powers at reverse bias voltage (a)  $V_b = 0$  V and (b)  $V_b = 15$  V; corresponding photocurrent spectra at (c) 0 V and (d) 15 V bias voltage.

Here we model the dependence of the photocurrent on the optical power in the microring using the power law,  $I_{ph} = \xi P_r^m$ , with  $1 \leq m \leq 2$ . The optical power  $P_r$  in the microring and the transmitted power  $P_{out}$  in the output waveguide are given by [4]

$$P_r = \frac{P_{r,max}}{1 + F \sin^2[(\phi_L + \phi_{NL})/2]}, \quad (1)$$

$$\frac{P_{out}}{P_{in}} = \frac{T_{min} + F \sin^2[(\phi_L + \phi_{NL})/2]}{1 + F \sin^2[(\phi_L + \phi_{NL})/2]}, \quad (2)$$

where  $P_{r,max} = \kappa^2 P_{in} / (1 - \tau a_{rt})^2$  is the peak power in the microring,  $\tau = \sqrt{1 - \kappa^2}$  is the transmission coefficient of the coupling junction,  $F = 4\tau a_{rt} / (1 - \tau a_{rt})^2$  is the contrast factor of the resonator, and

$$T_{min} = \frac{(\tau - a_{rt})^2}{(1 - \tau a_{rt})^2} \quad (3)$$

is the minimum power transmission of the resonance spectrum. From Eq. (2), we find that the minimum transmission occurs when the linear phase detune is equal to the negative of the nonlinear phase,  $\phi_{L,min} = -\phi_{NL}^*$ . This is also the point where the power in the microring reaches the maximum value,  $P_r = P_{r,max}$ , as seen from Eq. (1), which gives rise to the peak photocurrents in the spectra in Figs. 3(c) and 3(d). Thus, by measuring the wavelength shift  $\Delta\lambda_{min}$  of the minimum transmission point relative to the linear resonance, we can determine the nonlinear phase  $\phi_{NL}^*$  corresponding to  $P_{r,max}$  in the microring as

$$\phi_{NL}^* = -\phi_{L,min} = 2\pi(\Delta\lambda_{min}/\text{FSR}). \quad (4)$$

Also, from the minimum power transmission,  $T_{min}$ , we can calculate the total round-trip attenuation  $a_{rt}$  using Eq. (3) as  $a_{rt} = (\tau + \sqrt{T_{min}}) / (1 + \tau\sqrt{T_{min}})$ . The total loss coefficient in the microring waveguide can then be obtained from  $\alpha = -\ln(a_{rt})/\pi R = \alpha_L + (L_{PD}/2\pi R)\alpha_{NL}$ , where  $\alpha_L$  is the linear loss coefficient (which includes linear absorption, DSA, FC absorption, and scattering) and  $\alpha_{NL}$  is the nonlinear loss due to TPA and absorption from the TPA-generated FC.

Figure 4(a) plots the total loss coefficient  $\alpha$  as a function of the peak power  $P_{r,max}$  in the microring for reverse bias voltages of 0, 13, and 15 V. We observe that the total loss coefficient does not vary significantly with the peak power, indicating that the nonlinear loss contribution from TPA is small compared to the linear loss. We can thus neglect nonlinear absorption effect in the microring. Figure 4(b) plots the dependence of the peak photocurrent  $I_{ph,max}$  on the peak optical power  $P_{r,max}$  in the microring. We observe that  $I_{ph,max}$  varies almost quadratically ( $m = 1.98$ ) with the optical power at 0 V bias, indicating that FC generation by TPA dominates at low bias voltages. This dependence becomes increasingly more linear (with  $m$  approaching 1) at high reverse bias voltages close to breakdown, which suggests that DSA becomes more dominant in this regime. In Fig. 4(c), we plot the nonlinear phase  $\phi_{NL}^*$  as a function of the peak photocurrent  $I_{ph,max}$  at 13 V and 15 V bias voltages, with the curve for 0 V bias shown in the inset. The plot shows that the nonlinear phase varies approximately as the square root of the current at 0 V bias but becomes linearly dependent on  $I_{ph,max}$  at high reverse bias voltages. At a high bias



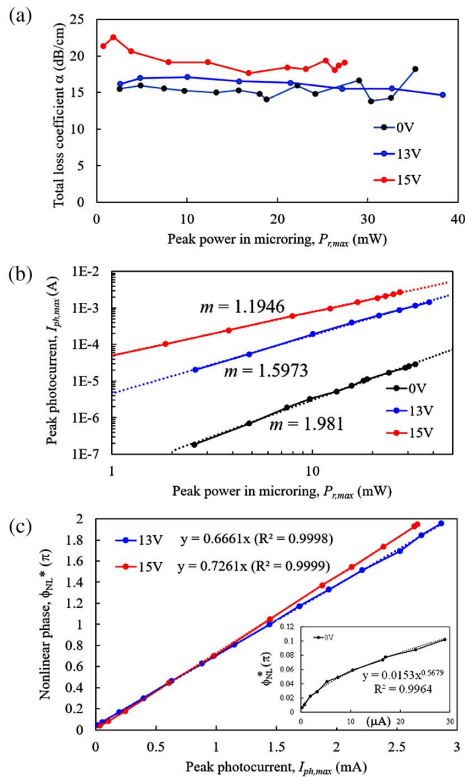


**Fig. 4.** (a) Plot of the total loss coefficient  $\alpha$  versus peak optical power  $P_{r,\max}$  in the microring at reverse bias voltages of 0, 13, and 15 V; (b) dependence of the peak photocurrent  $I_{ph,\max}$  on the peak power  $P_{r,\max}$ ; dotted lines are best-curve fits of the log-log plots with slope  $m$ . (c) Linear dependence of the nonlinear phase  $\phi_{NL}^*$  on the peak photocurrent  $I_{ph,\max}$  at 13 V and 15 V bias voltages. Inset plot shows the curve for 0 V bias.

voltage  $V_b$  which results in a large photocurrent, the temperature change in the Si waveguide core is directly proportional to the power dissipated by the photocurrent,  $\Delta T \propto V_b I_{ph}$ . The refractive index change due to the thermo-optic effect is thus also linearly proportional to the current,  $\Delta n = K \Delta T \propto V_b I_{ph}$ , where  $K$  is the thermo-optic coefficient of Si. This results in the observed linear relationship between the nonlinear phase and photocurrent at high reverse bias in Fig. 4(c). On the other hand, at 0 V bias, where the photocurrent is significantly smaller and consists mainly of the diffusion component, the thermo-optic change of the refractive index depends on the optical power in the microring,  $\Delta n \propto P_{r,\max}$ . Since the photocurrent varies quadratically with  $P_{r,\max}$  near zero bias, we obtain the square root dependence of the nonlinear phase on the photocurrent.

The results in Fig. 4(c) indicate a giant thermo-optic nonlinear effect in the MR APD, which can cause the nonlinear phase to exceed  $2\pi$  at high reverse bias voltages and high input optical powers. This effect can also be seen in the photocurrent spectrum at 15 V bias voltage and 1.86 mW input optical power in Fig. 5, which shows that the peak photocurrent is shifted by 5.13 nm compared to the microring's linear FSR of 4.67 nm measured at low optical power (46  $\mu$ W). Effectively, the large thermo-optic nonlinearity causes the microring's FSR

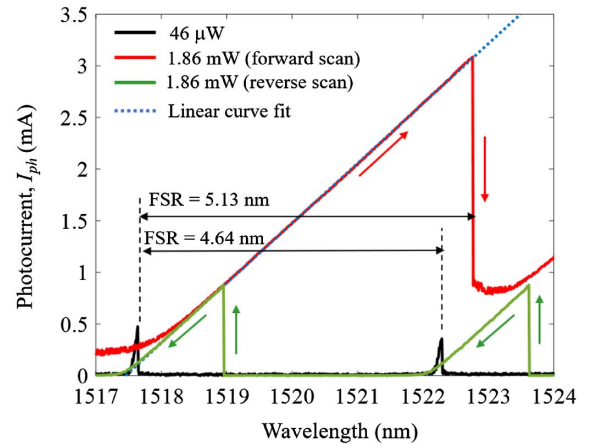


**Fig. 5.** Variations of the photocurrent with wavelength of the MR APD at 15 V reverse bias voltage; black curve is the response at low input optical power (46  $\mu$ W) multiplied by a factor of 10 to make it visible; red and green curves are the responses at high input optical power (1.86 mW) obtained from forward and reverse wavelength scans, respectively. The dotted line is the best linear fit to the forward photocurrent spectrum over the 1518.5–1522.5 nm wavelength range.

to expand at high optical powers. To our knowledge, such giant thermo-optic nonlinearity induced by only a few milliwatts of input optical power has not been reported before in a Si microring resonator. By contrast, Fig. 3(c) shows that at 0 V bias, the same level of input optical powers induces a resonance shift of only a tiny fraction of the FSR. If we define a nonlinear coefficient  $n_{2,TO}$  due to the thermo-optic effect such that the nonlinear index change is given by  $\Delta n_{NL} = n_{2,TO}(P_r/A_{eff})$ , where  $A_{eff} = 0.20 \mu\text{m}^2$  is the effective mode area of the Si rib waveguide, we obtain  $n_{2,TO} = 0.63 \text{ cm}^2/\text{GW}$  at 15 V, which is a 20 times enhancement over the value  $n_{2,TO} \approx 0.028 \text{ cm}^2/\text{GW}$  at 0 V. For comparison, the nonlinear refractive index due to the Kerr effect in Si is about 4 orders of magnitude smaller ( $n_2 = 4.5 \times 10^{-5} \text{ cm}^2/\text{GW}$ ) [19]. The giant thermo-optic nonlinearity in our device is the direct result of the large photocurrent generated in the  $p^+pn^+$  junction near breakdown.

Another remarkable feature of the photocurrent spectrum in Fig. 5 is that the current varies linearly with the wavelength over the microring's FSR, with a sensitivity slope of 0.576 mA/nm and linear correlation coefficient  $R = 0.9999$  over 1518.5–1522.5 nm. Similar linear photocurrent spectra are also observed in Fig. 3(d) at high reverse bias voltages and high input optical powers. This linear behavior is a consequence of the large contrast factor  $F$  of the microring resonator and the linear dependence of the photocurrent on the optical power in the microring at high bias voltages, which can be shown as follows. Since  $\phi_{NL} = \gamma I_{ph}^n$  and  $I_{ph} = \xi P_r^m$ , we can write  $P_r/P_{r,\max} = (\phi_{NL}/\phi_{NL}^*)^\nu$ , where  $\nu = 1/mn$ . Substituting this expression into Eq. (1) and differentiating the equation with respect to the linear phase  $\phi_L$ , we can solve for the change of the nonlinear phase with respect to  $\phi_L$  to get

$$\frac{d\phi_{NL}}{d\phi_L} = \frac{-F \sin \phi_{rt}}{F \sin \phi_{rt} + \frac{2\nu}{\phi_{NL}} \left(\frac{\phi_{NL}}{\phi_{NL}^*}\right)^\nu}. \quad (5)$$

For large  $F$  ( $\sim 2900$  for our device), the second term in the denominator on the right-hand side is much smaller than the first term for large round-trip phase  $\phi_{rt}$ , so that the nonlinear phase varies linearly with the linear phase detune with a slope  $d\phi_{NL}/d\phi_L \approx -1$  independent of the exponent  $\nu$ . This results in a linear photocurrent spectrum at high reverse bias voltages, where the nonlinear phase varies almost linearly with the photocurrent. Enhanced by the large thermo-optic nonlinearity, the linear photocurrent spectrum spans the entire FSR of the microring, providing unique wavelength-resolved photodetection characteristics that could enable novel applications, as briefly discussed in the next section. It should be mentioned that at high input optical powers, the resonance spectrum exhibits a bistable effect so that there is a hysteresis between the forward and reverse wavelength scans, as can be seen in Fig. 5, with a lower wavelength detune threshold  $\Delta\lambda$  of 1.31 nm from the cavity resonance (for switching from lower branch to upper branch) and upper threshold of 5.13 nm (for switching from upper branch to lower branch). This means that in order to reach the upper hysteresis branch, one would need to start from a shorter wavelength or a lower power point, and then increase the wavelength or ramp up the power.

The large photogenerated currents also lead to very high responsivities for the MR APD at high reverse bias voltages near breakdown. In Fig. 6, we plot the peak responsivity, defined as  $R_{max} = I_{ph,max}/P_{in}$ , at 13 and 15 V bias voltages. We observe that peak responsivity values above 1 A/W can be achieved at 15 V bias for input optical powers as small as 0.2 mW, reaching a value of 1.5 A/W at 1.5 mW optical power. This is comparable to the performance of Ge-Si PDs [20,21] and to our knowledge, such high responsivities have not been reported for CMOS-compatible Si PDs at telecom wavelengths before. Even higher responsivities can be achieved if we increase the reverse bias voltage and drive the PD deeper into the avalanche region. We also plot in Fig. 6 the ratio of the photocurrent to the dark current as a function of the input optical power at 13 and 15 V bias voltages. Due to the relatively low dark currents at these bias voltages, we obtain very high photo-to-dark current ratios in the order of  $10^6$ .

Although our MR APD was not optimized for high-speed operation, we also performed time-domain measurements to estimate the device's time response to input optical pulses.

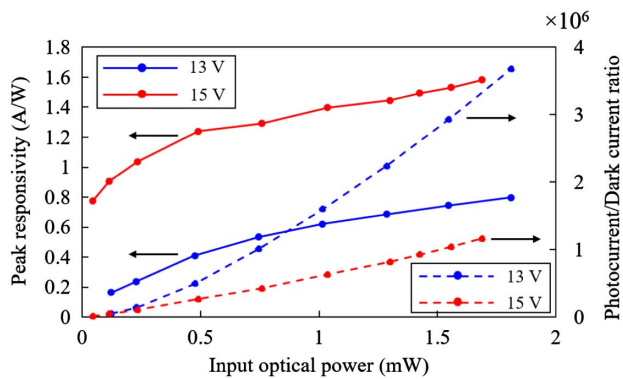


**Fig. 6.** Peak responsivity and ratio of the peak photocurrent to dark current of the MR APD as functions of the input optical power at 13 and 15 V reverse bias voltages.

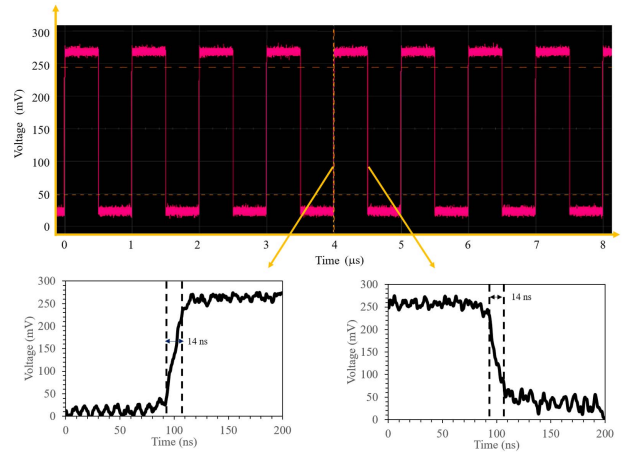


**Fig. 7.** Detected photocurrent waveform (converted to voltage) for a square-wave optical input signal of 1 MHz frequency; lower panels are the zoomed-in views of the rising and falling edges of the waveform.

We biased the MR APD at 15 V and applied an input optical signal of 1 mW power at 1523.2 nm wavelength ( $\sim 1$  nm detuned from the linear resonance) with its amplitude modulated by a 1 MHz square wave with rise/fall times  $\approx 10$  ns. The output photocurrent was converted into voltage using a transimpedance amplifier (TIA) and fed to an oscilloscope. Figure 7 shows the detected photocurrent waveform, from which we obtain rise time and fall time of 14 ns for the photocurrent response. Thus the MR APD response time is adequate for low-speed applications (10s MHz) such as spectrometry, power monitoring, frequency-chirped source characterization, and sensing, as discussed below.

#### 4. DISCUSSION AND CONCLUSION

The unique linear photocurrent spectrum of the MR APD spanning the full FSR could enable many interesting applications, especially given the compact size of the device. Here we briefly propose three potential applications. As the first application, the MR APD may be used for wavelength-resolved photodetection as a compact on-chip spectrometer. For example, the device can be used to monitor or identify the wavelengths of optical signals in a wavelength division multiplexing network. Since the MR APD is sensitive to both the wavelength and optical power, a separate photodetector would be required to independently determine the power of the optical signal, which is then used along with the MR APD photocurrent to accurately determine its wavelength. Another application that takes advantage of the linear photocurrent spectrum of the MR APD is characterization of linear frequency chirped laser sources, such as those used in lidars. The conventional approach for measuring linear frequency chirp is to use a Mach-Zehnder interferometer and PDs [22,23]. Here the MR APD could offer a simpler and much more compact solution. Finally, the device can be used as a refractometric sensor by detecting the change in the photocurrent in response to a change in the effective index of the microring resonator in the presence of an analyte. Due to the very broad band of the

photocurrent spectrum, such a sensor would not require a laser source with precise wavelength tuning as in conventional microring sensors [24,25].

To summarize, we demonstrated a fully CMOS-compatible Si photodetector using a  $p^+pn^+$  junction embedded in a microring resonator. Operated under avalanche condition, we obtained large photocurrents generated predominantly from the linear DSA, achieving high responsivities exceeding 1 A/W at telecommunication wavelengths. The large photocurrents also give rise to giant thermo-optic nonlinear effects in the microring resonator, resulting in linear photocurrent spectra spanning the entire FSR of the resonator. We also proposed several potential applications that exploit this unique behavior of the MR APD.

**Funding.** Natural Sciences and Engineering Research Council of Canada.

**Disclosures.** The authors declare no conflicts of interest.

**Data Availability.** Data underlying the results presented in this paper may be obtained from the authors upon reasonable request.

## REFERENCES

- M. Huang, P. Cai, S. Li, G. Hou, N. Zhang, T.-I. Su, C.-Y. Hong, and D. Pan, "56 GHz waveguide Ge/Si avalanche photodiode," in *Optical Fiber Communications Conference and Exposition (OFC)* (2018), pp. 1–3.
- C.-L. Hsin, S.-M. Wang, G.-Y. Chen, M.-H. Wu, C.-W. Huang, S.-C. Hsu, and S.-C. Lo, "Si/Ge/Si photodetector by rapid-melting-growth technique," *IEEE Trans. Nanotechnol.* **17**, 607–610 (2018).
- J. Cui and Z. Zhou, "High-performance Ge-on-Si photodetector with optimized DBR location," *Opt. Lett.* **42**, 5141–5144 (2017).
- Y. Ren and V. Van, "Enhanced small-signal responsivity in silicon microring photodetector based on two-photon absorption," *IEEE J. Sel. Top. Quantum Electron.* **26**, 3800208 (2020).
- J. Bradley, P. Jessop, and A. Knights, "Silicon waveguide-integrated optical power monitor with enhanced sensitivity at 1550 nm," *Appl. Phys. Lett.* **86**, 241103 (2005).
- J. J. Ackert, A. S. Karar, D. J. Paez, P. E. Jessop, J. C. Cartledge, and A. P. Knights, "10 Gbps silicon waveguide-integrated infrared avalanche photodiode," *Opt. Express* **21**, 19530–19537 (2013).
- M. W. Geis, S. J. Spector, M. E. Grein, J. U. Yoon, D. M. Lennon, and T. M. Lyszczarz, "Silicon waveguide infrared photodiodes with >35 GHz bandwidth and phototransistors with 50 A/W response," *Opt. Express* **17**, 5193–5204 (2009).
- X. Mao, P. Han, L. Gao, Y. Mi, S. Hu, Y. Fan, C. Zhao, and Q. Wang, "Selenium-doped silicon-on-insulator waveguide photodetector with enhanced sensitivity at 1550 nm," *IEEE Photon. Technol. Lett.* **23**, 1517–1519 (2011).
- S. T. Fard, K. Murray, M. Caverley, V. Donzella, J. Flueckiger, S. M. Grist, E. Huante-Ceron, S. A. Schmidt, E. Kwok, N. A. F. Jaeger, A. P. Knights, and L. Chrostowski, "Silicon-on-insulator sensors using integrated resonance-enhanced defect-mediated photodetectors," *Opt. Express* **22**, 28517–28529 (2014).
- R. R. Grote, K. Padmaraju, B. Souhan, J. B. Driscoll, K. Bergman, and R. M. Osgood, "10 Gb/s error-free operation of all-silicon ion-implanted-waveguide photo diodes at 1.55  $\mu\text{m}$ ," *IEEE Photon. Technol. Lett.* **25**, 67–70 (2012).
- B. Desiatov, I. Goykhman, J. Shappir, and U. Levy, "Defect-assisted sub-bandgap avalanche photodetection in interleaved carrier-depletion silicon waveguide for telecom band," *Appl. Phys. Lett.* **104**, 091105 (2014).
- Y. Li, S. Feng, Y. Zhang, and A. W. Poon, "Sub-bandgap linear-absorption-based photodetectors in avalanche mode in PN-diode-integrated silicon microring resonators," *Opt. Lett.* **38**, 5200–5203 (2013).
- X. Li, Z. Li, X. Xiao, H. Xu, J. Yu, and Y. Yu, "40 Gb/s all-silicon photodetector based on microring resonators," *IEEE Photon. Technol. Lett.* **27**, 729–732 (2015).
- K. Nisbida, K. Taguchi, and Y. Matsumoto, "InGaAsP heterostructure avalanche photodiodes with high avalanche gain," *Appl. Phys. Lett.* **35**, 251–252 (1979).
- B. Souhan, R. R. Grote, J. B. Driscoll, and R. M. Osgood, "Ion-implanted silicon-waveguide avalanche photodiode with separate absorption-multiplication region for C-band operation," in *Frontiers in Optics* (2012), paper FTu2A–5.
- <https://www.lumerical.com/products/mode/>.
- R. Van Overstraeten and H. De Man, "Measurement of the ionization rates in diffused silicon P-N junctions," *Solid-State Electron.* **13**, 583–608 (1970).
- W. Maes, K. De Meyer, and R. Van Overstraeten, "Impact ionization in silicon: a review and update," *Solid-State Electron.* **33**, 705–718 (1990).
- M. Dinu, F. Quochi, and H. Garcia, "Third-order nonlinearities in silicon at telecom wavelengths," *Appl. Phys. Lett.* **82**, 2954–2956 (2003).
- S. A. Srinivasan, M. Berciano, P. De Heyn, S. Lardenois, M. Pantouvaki, and J. Van Campenhout, "27 GHz silicon-contacted waveguide-coupled Ge/Si avalanche photodiode," *J. Lightwave Technol.* **38**, 3044–3050 (2020).
- Z. Su, E. S. Hosseini, E. Timurdogan, J. Sun, M. Moresco, G. Leake, T. N. Adam, D. D. Coolbaugh, and M. R. Watts, "Whispering gallery germanium-on-silicon photodetector," *Opt. Lett.* **42**, 2878–2881 (2017).
- S. N. Zheng, J. Zou, H. Cai, J. Song, L. Chin, P. Liu, Z. Lin, D. Kwong, and A. Liu, "Microring resonator-assisted Fourier transform spectrometer with enhanced resolution and large bandwidth in single chip solution," *Nat. Commun.* **10**, 2349 (2019).
- J. Yang, T. Yang, Z. Wang, D. Jia, and C. Ge, "A novel method of measuring instantaneous frequency of an ultrafast frequency modulated continuous-wave laser," *Sensors* **20**, 3834 (2020).
- G. Mi, C. Horvath, M. Aktary, and V. Van, "Silicon microring refractive index sensor for atmospheric CO<sub>2</sub> gas monitoring," *Opt. Express* **24**, 1773–1780 (2016).
- W. Huang, Y. Luo, W. Zhang, C. Li, L. Li, Z. Yang, and P. Xu, "High-sensitivity refractive index sensor based on Ge–Sb–Se chalcogenide microring resonator," *Infrared Phys. Technol.* **116**, 103792 (2021).